Electronic Supplementary Information

Incorporation of nickel single atoms into carbon paper as self-standing electrocatalyst for CO$_2$ reduction

Simin Li[a], Marcel Ceccato[a], Xiuyuan Lu[b], Sara Frank[a], Nina Lock[c], Alberto Roldan[b], Xin-Ming Hu[a,d,*], Troels Skrydstrup[a], and Kim Daasbjerg[a,*]

[a] Carbon Dioxide Activation Center (CADIAC), Interdisciplinary Nanoscience Center (iNANO), and Department of Chemistry
Aarhus University
Gustav Wieds Vej 14, 8000 Aarhus, Denmark
Email: kdaa@chem.au.dk

[b] Cardiff Catalysis Institute, School of Chemistry
Cardiff University
Main Building, Park Place, Cardiff, CF10 3AT, UK

[c] Carbon Dioxide Activation Center (CADIAC), Department of Engineering
Aarhus University
Åbogade 40, 8200 Aarhus N, Denmark

[d] Environment Research Institute
Shandong University
Binhai Road 72, Qingdao 266237, China.
Email: huxm@sdu.edu.cn
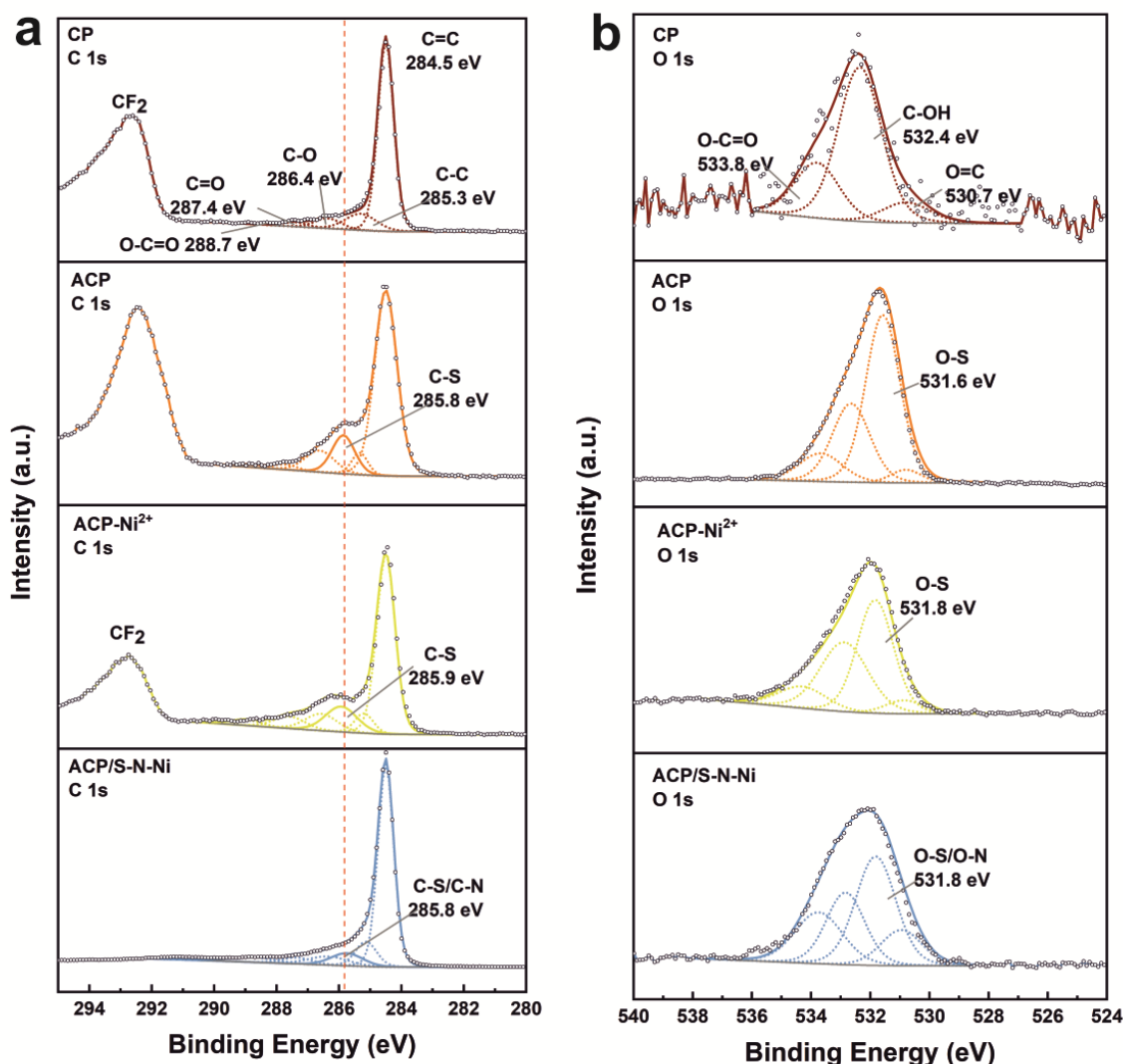
Figure S1. (a) High resolution XPS spectra of C 1s and (b) O 1s of the materials obtained at each step in the synthesis of ACP/S-N-Ni.

Figure S1a displays the high resolution C 1s spectra of the materials obtained at each step in the synthesis of ACP/S-N-Ni. For raw CP the peaks at 284.5 and 285.3 eV are ascribed to sp^2 (C=C) and sp^3 (C–C) carbon, respectively. The small peaks at higher binding energies are related to C–O ($\sim$286.5 eV), C=O ($\sim$287.6 eV), and O–C=O ($\sim$288.9 eV). In addition, an intense peak at $\sim$292.6 eV is attributed to CF$_2$, stemming from the polytetrafluoroethylene used to treat the as-received CP. After acid treatment to afford ACP, XPS reveals a new shoulder at $\sim$285.8 eV, corresponding to C-SO$_3^-$.[S1, 2] The subsequent adsorption of Ni^{2+} to produce ACP-Ni^{2+} does not cause obvious changes in these peaks. After pyrolysis in the presence of urea, the shoulder

pertaining to C-SO$_3^-$ disappears on ACP/S-N-Ni. Instead, a peak attributed to C-S/C-N emerges. Moreover, the CF$_2$ peak disappears, suggesting that the F atoms are completely removed.

Figure S1b shows the high resolution O 1s spectra at the same stages of the synthesis. For pristine CP, the peaks at 530.7, 532.4, and 533.8 eV are ascribed to carbonyl (C=O), hydroxyl (C−OH) and ester (O−C=O), respectively. After acid treatment, an additional peak at 531.6 eV appears for ACP, attributed to O−S^2 and in agreement with the deconvolution of the S 2p spectrum (see **Figure 2c**). Moreover, the intensity of the O 1s spectrum increases notably after acid activation (content of O increases from 0.2 to 5.7 at%; see also **Table S2**).
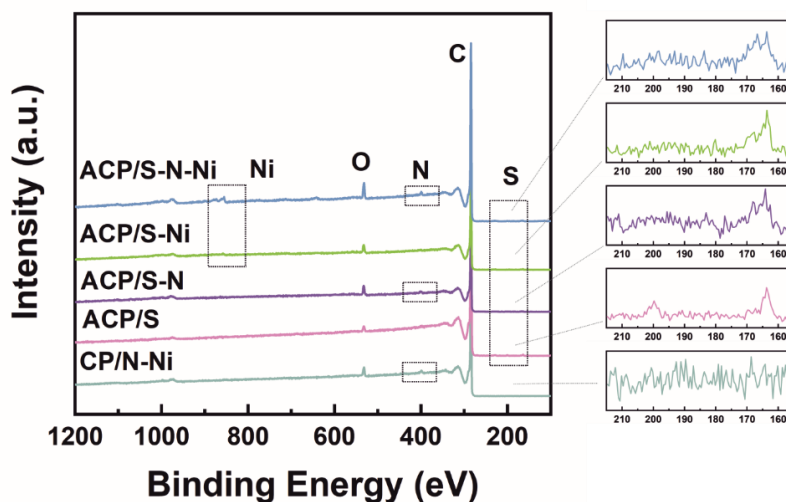
Figure S2. XPS survey spectra of CP/N-Ni, ACP/S, ACP/S-N, ACP/S-Ni, and ACP/S-N-Ni.

Figure S2 displays the XPS survey spectra of the electrodes used in this work. The electrodes all consist of mainly carbon and a small amount of oxygen. In addition, a S signal, appears for all electrodes, the exception being CP/N-Ni due to the lack of acid treatment in this case. In accordance with expectations, N and Ni signals are seen on the electrodes where N and/or Ni were introduced during the synthesis.
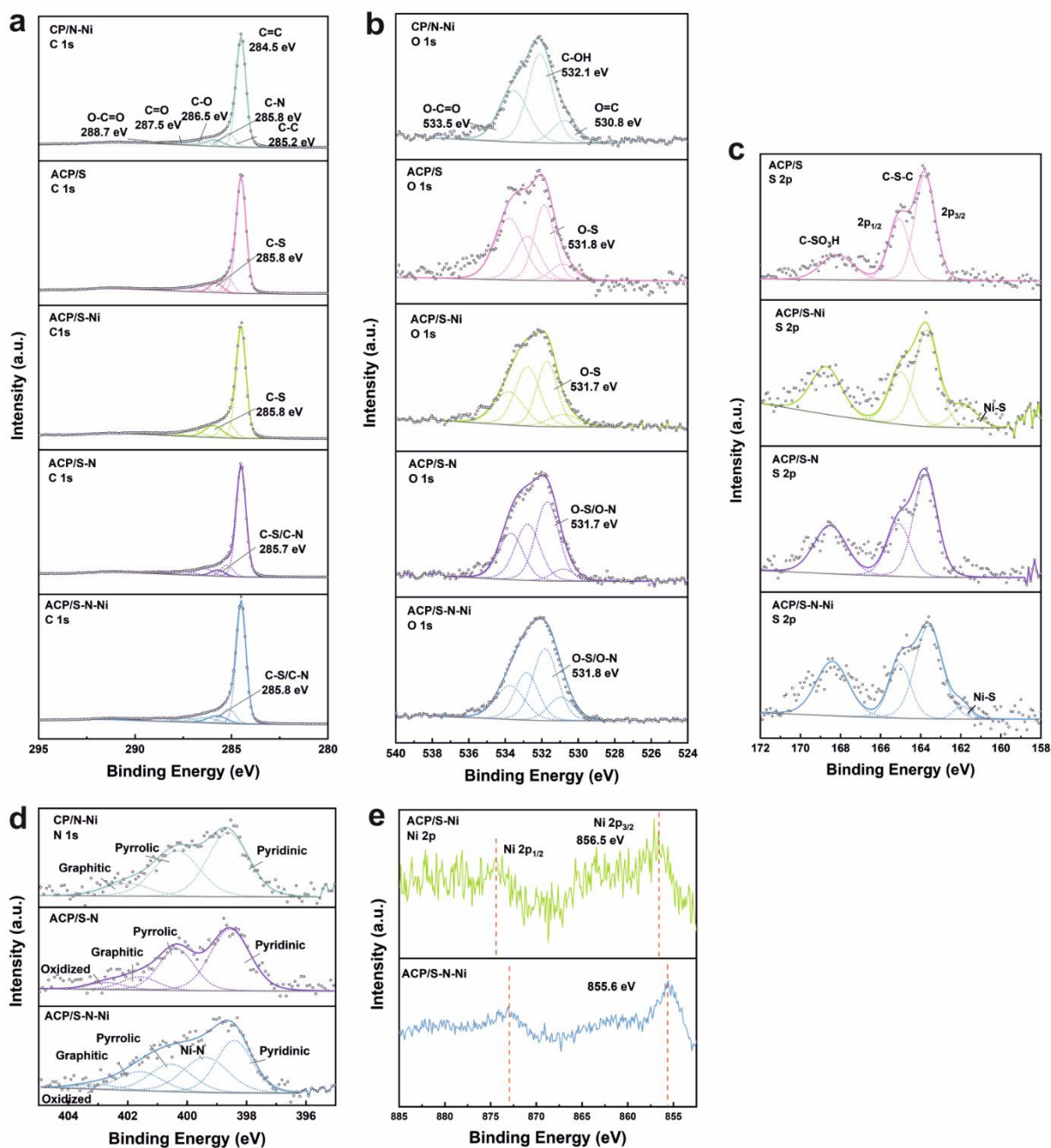
Figure S3. (a) High resolution XPS spectra of C 1s, (b) O 1s, (c) S 2p, (d) N 1s, and (e) Ni 2p of CP/N-Ni, ACP/S, ACP/S-Ni, ACP/S-N, and ACP/S-N-Ni.

Figure S3a presents the high resolution XPS C 1s spectra of CP/N-Ni, ACP/S, ACP/S-Ni, ACP/S-N, and ACP/S-N-Ni. In general, they all show two major peaks at 284.5 and 285.2 eV, which are ascribed to sp^2 (C=C) and sp^3 (C–C) carbon, respectively. Three smaller peaks at 286.5, 287.5, and 288.7 eV are attributed to C–O, C=O, and O–C=O, respectively. A sixth peak at 285.8 eV can be assigned to C-N and/or C-S bonds of similar binding energies.

Figure S3b displays the high resolution XPS O 1s spectra of CP/N-Ni, ACP/S, ACP/S-Ni, ACP/S-N, and ACP/S-N-Ni. The CP/N-Ni electrode shows three peaks at 530.8, 532.1 and 533.5 eV, which are ascribed to carbonyl (C=O), hydroxyl (C−OH), and ester (O−C=O), respectively. The ACP/S, ACP/S-N, ACP/S-Ni, and ACP/S-N-Ni electrodes exhibit the same three peaks as well as a new peak at ~531.8 eV corresponding to O−N and/or O−S bonds. In addition, S is introduced for all the electrodes undergoing acid treatment (i.e. ACP/S, ACP/S-N, ACP/S-Ni, and ACP/S-N-Ni; **Figure S3c**). The S signals are mainly assigned to two types of species, where thienyl S (163.7 and 165.0 eV) is the major one and sulfonic acid groups (168.5 eV) the minor one. Note that a weak Ni-S bond is also observed in ACP/S-Ni and ACP/S-N-Ni.

Figure S3d displays the high resolution XPS N 1s spectra of CP/N-Ni, ACP/S-N, and ACP/S-N-Ni. The CP/N-Ni electrode contains pyridinic, pyrrolic, and graphitic N species. The same three types of N species are present in ACP/S-N and ACP/S-N-Ni. Furthermore, ACP/S-N exhibits one more oxidized N species, while ACP/S-N-Ni has oxidized N and N-Ni species.

Figure S3e presents the high resolution XPS Ni 2p spectra of the two electrodes containing Ni, i.e. ACP/S-Ni and ACP/S-N-Ni. The former electrode shows a slightly higher Ni binding energy than the latter, indicating the different chemical environment of Ni in the two electrodes. This is not surprising as the Ni in ACP/S-Ni mainly binds with S, while the Ni in ACP/S-N-Ni mainly coordinates with N, and only to a smaller extent with S. The different environment of Ni explains the inferior catalytic activity of ACP/S-Ni for eCO$_2$RR.
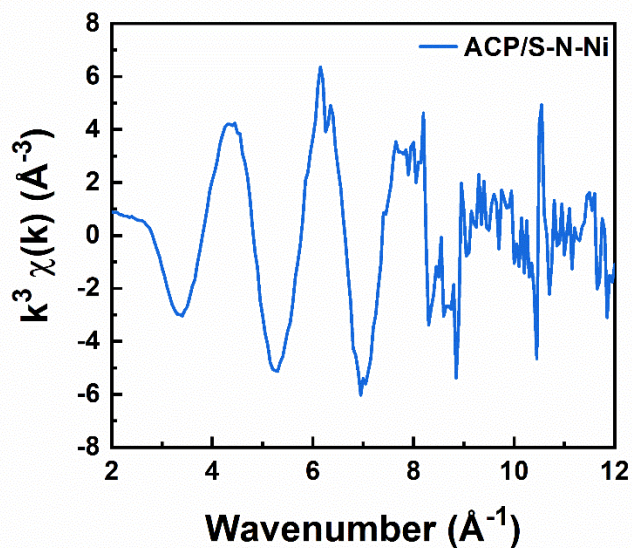
Figure S4. k^3-weighted k-space spectra of ACP/S-N-Ni.
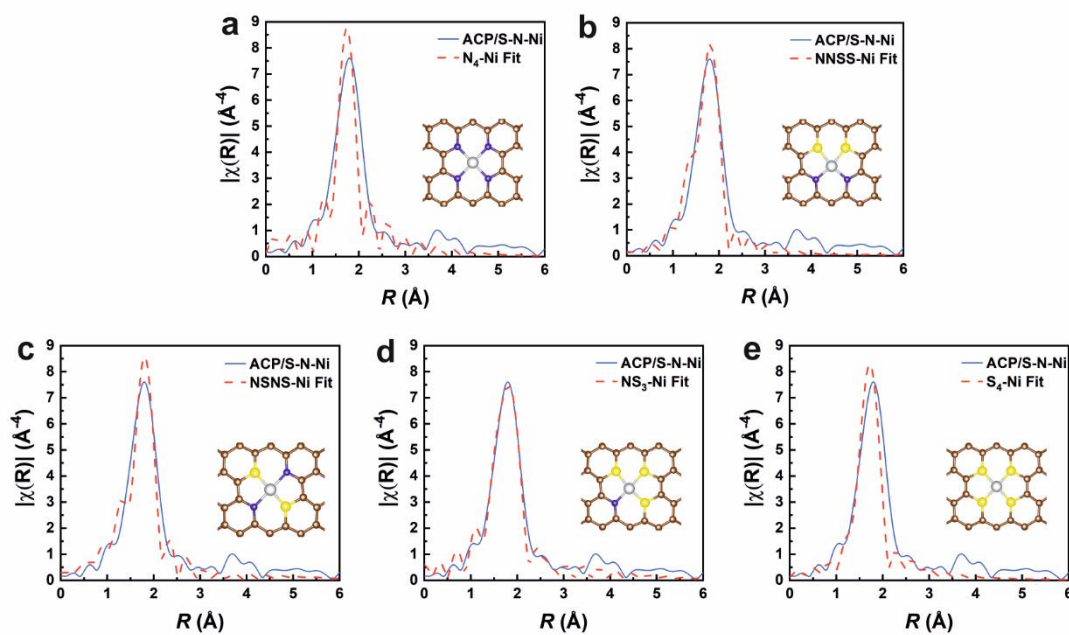
Figure S5. Proposed structures of the electrocatalytically active ACP/S-N-Ni material based on DFT calculations along with the corresponding fit of EXAFS data of ACP/S-N-Ni (see fitting details in **Table S1**). The grey, blue, yellow, and brown spheres represent Ni, N, S, and C atoms, respectively.
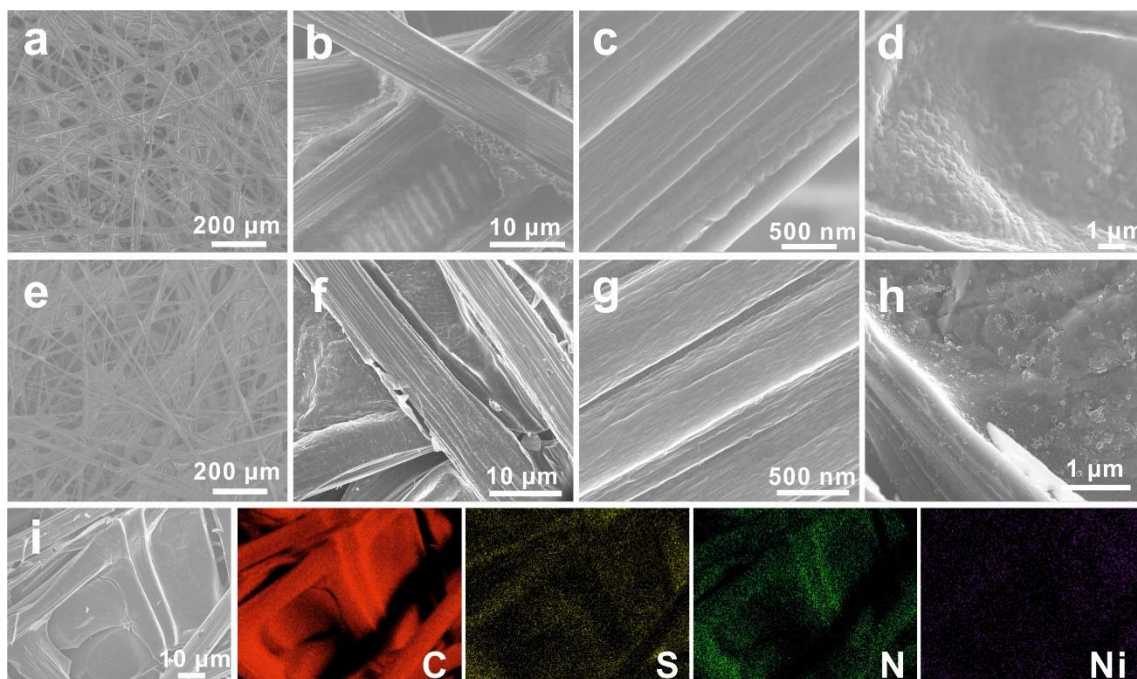
Figure S6. (a-d) SEM images of raw CP and (e-h) ACP/S-N-Ni at varying magnifications. (i) Corresponding element mapping of ACP/S-N-Ni by EDS equipped on SEM.
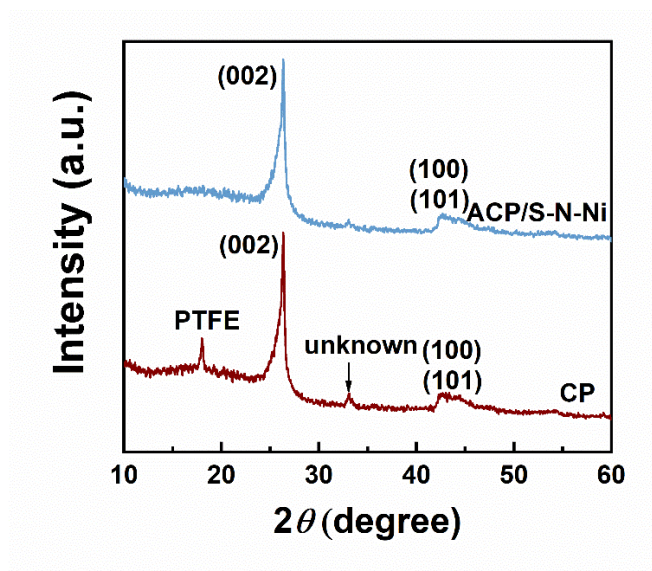
Figure S7. PXRD patterns of raw CP and ACP/S-N-Ni materials.

Figure S7 presents the PXRD patterns of the raw CP and ACP/S-N-Ni. Both electrodes show two peaks at ~26° and ~43°, which are indexed to the (002) as well as (100) and (101) planes of graphitic structure.[S3] A peak at ~18° in CP is attributed to polytetrafluoroethylene (PTFE),

originating from the as-received material. This is in line with the XPS analysis (**Figure 2b**). The PTFE peak disappears in ACP/S-N-Ni since PTFE thermally decomposes at high temperature.[S4] The PXRD pattern of ACP/S-N-Ni shows no peaks pertaining to any Ni species, indicating the absence of crystalline Ni-based particles.
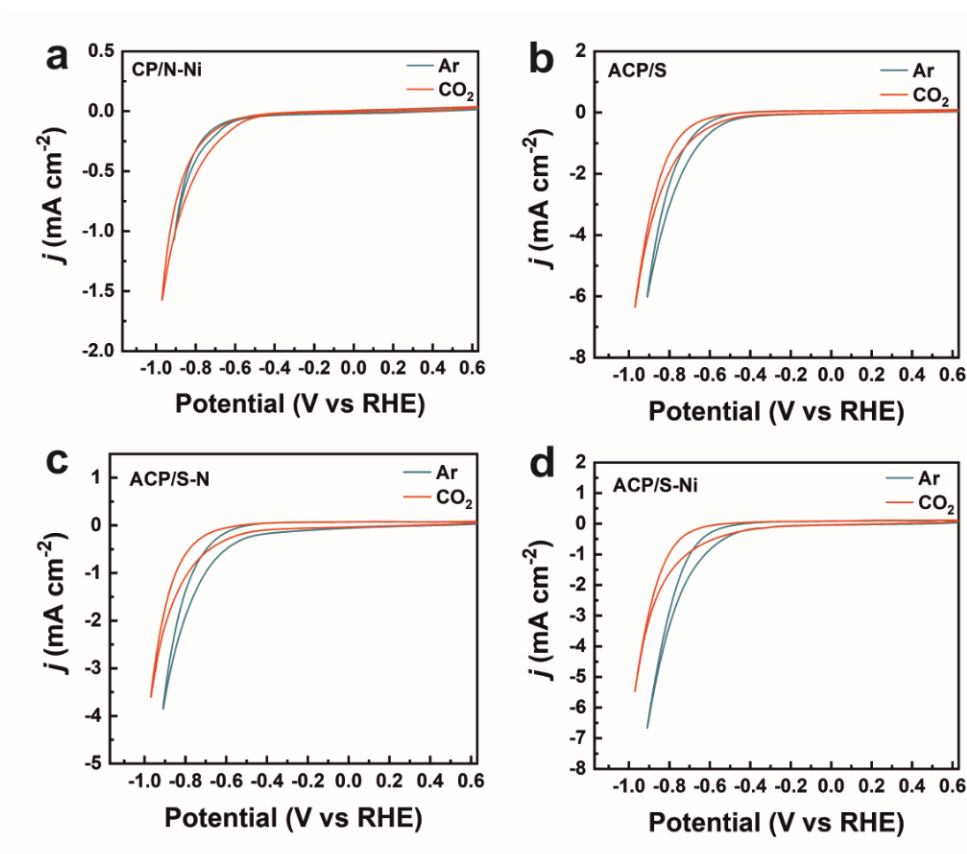
Figure S8. Cyclic voltammograms recorded at CP/N-Ni, ACP/S, ACP/S-N and ACP/S-Ni using $v = 10$ mV s^{-1} in 0.5 M KHCO$_3$.
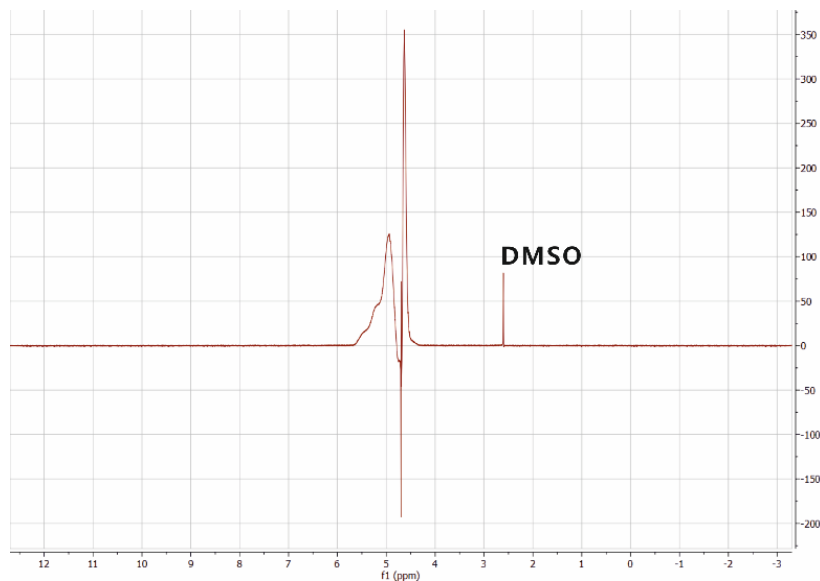
Figure S9. ^{1}H NMR spectra of the electrolyte after performing multiple electrolyses at potentials between -1.07 and -0.57 V vs RHE using ACP/S-N-Ni as working electrode in 0.5 M $KHCO_3$. No signal but the DMSO reference is observed, suggesting that no CO_2 reduction product is produced in the electrolyte.
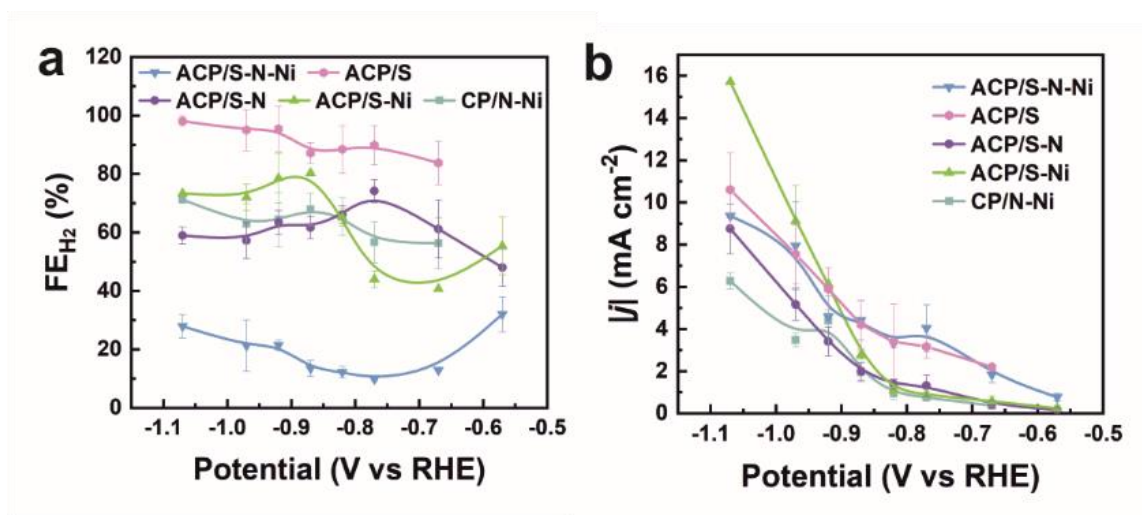
Figure S10. (a) FE_{H2} and (b) $|j|$ using CP/N-Ni, ACP/S, ACP/S-N, ACP/S-Ni, and ACP/S-N-Ni in 15 min electrolysis at various potentials in 0.5 M $KHCO_3$.
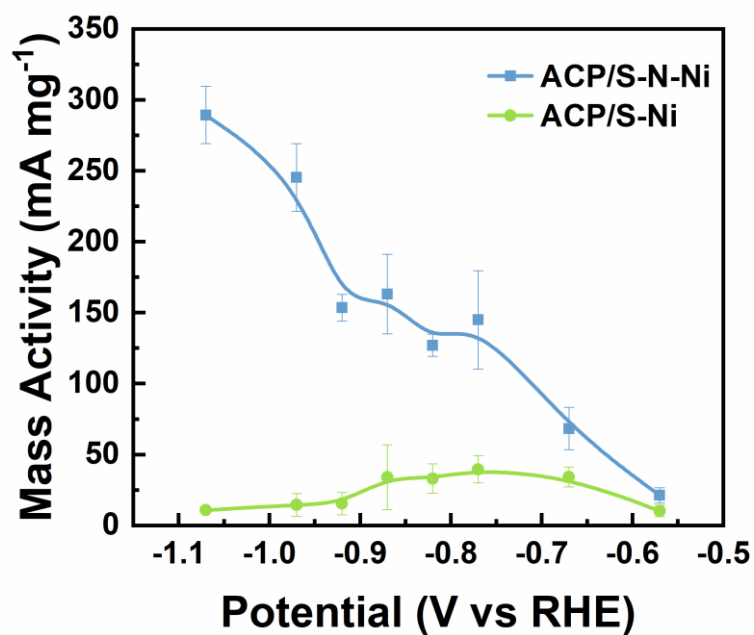
Figure S11. Mass activities relative to the Ni loading in ACP/S-N-Ni and APC/S-Ni.
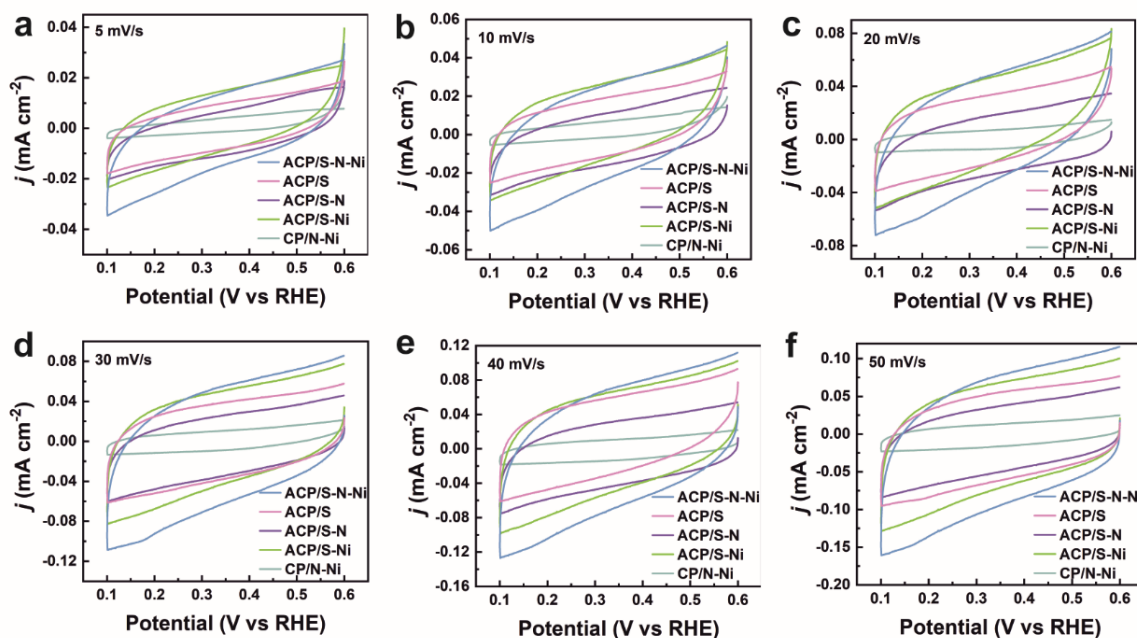
Figure S12. Cyclic voltammograms recorded at ACP/S-N-Ni, ACP/S, ACP/S-N, ACP/S-Ni, and CP/N-Ni between 0.1−0.6 V vs RHE using $v = 5, 10, 20, 30, 40,$ and 50 mV s^{-1} in CO$_2$-saturated 0.5 M KHCO$_3$.
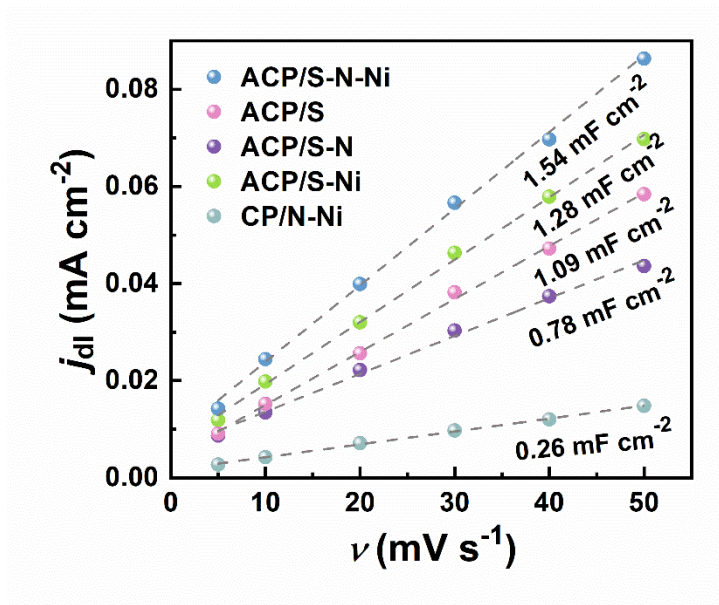
Figure S13. Plots of the double layer current density, j_{dl} (obtained at 0.35 V vs RHE from voltammograms in **Figure S15**), vs v.
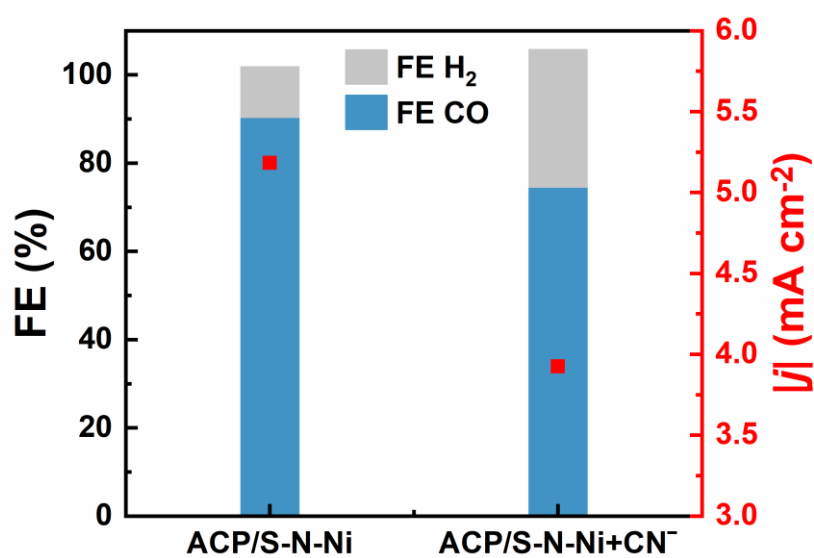
Figure S14. FE and $|j|$ measured at -0.77 V vs RHE for ACP/S-N-Ni in the absence/presence of 10 mM KCN in CO_2-saturated 0.5 M $KHCO_3$.
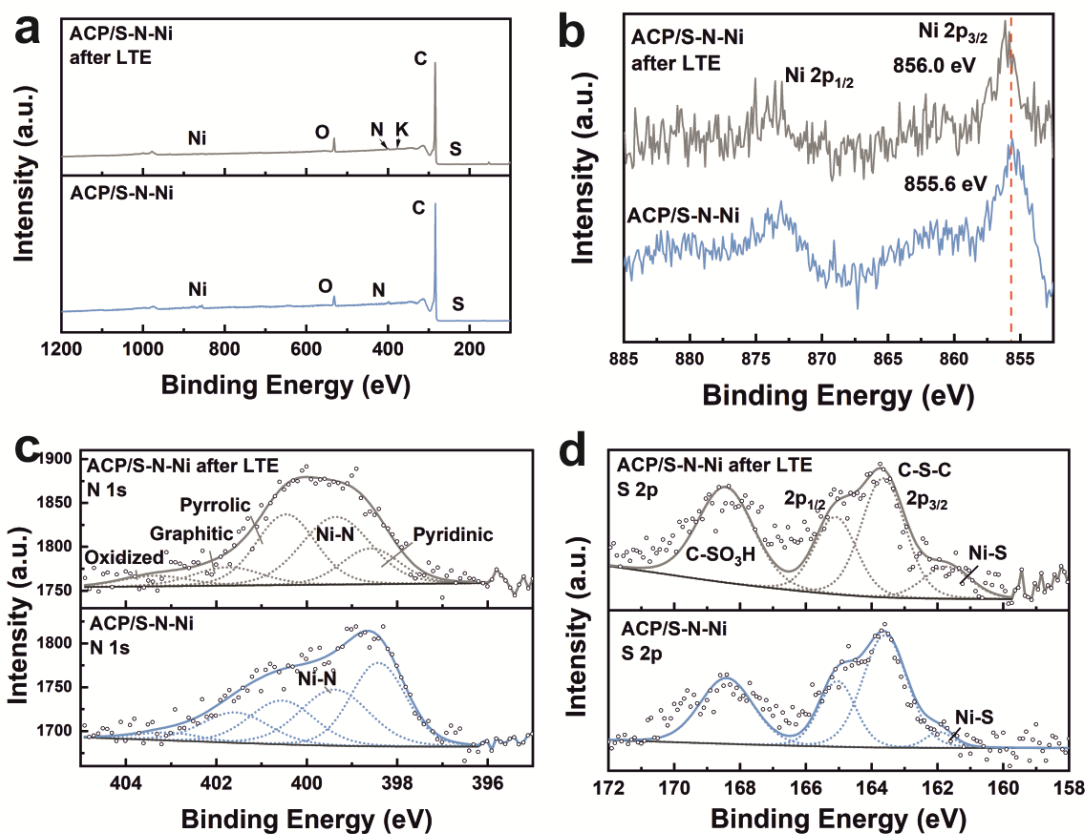
Figure S15. XPS spectra pertaining to the (a) survey, (b) Ni 2p, (c) N 1s, and (d) S 2p of ACP/S-N-Ni before and after 14 h electrolysis at −0.77 V vs RHE.

Figure S15 shows the XPS spectra recorded of the ACP/S-N-Ni electrode after 14 h electrolysis. Compared with the pristine one, a more intense peak from O and an additional peak from K are observed, stemming from residual amount of adsorbed $KHCO_3$ (from the electrolyte) on the carbon fiber surface. Otherwise, the changes observed in the Ni 2p, N 1s, and S 2p spectra are neglible after electrolysis, thus substantiating the high stability of the ACP/S-N-Ni electrode.

S13
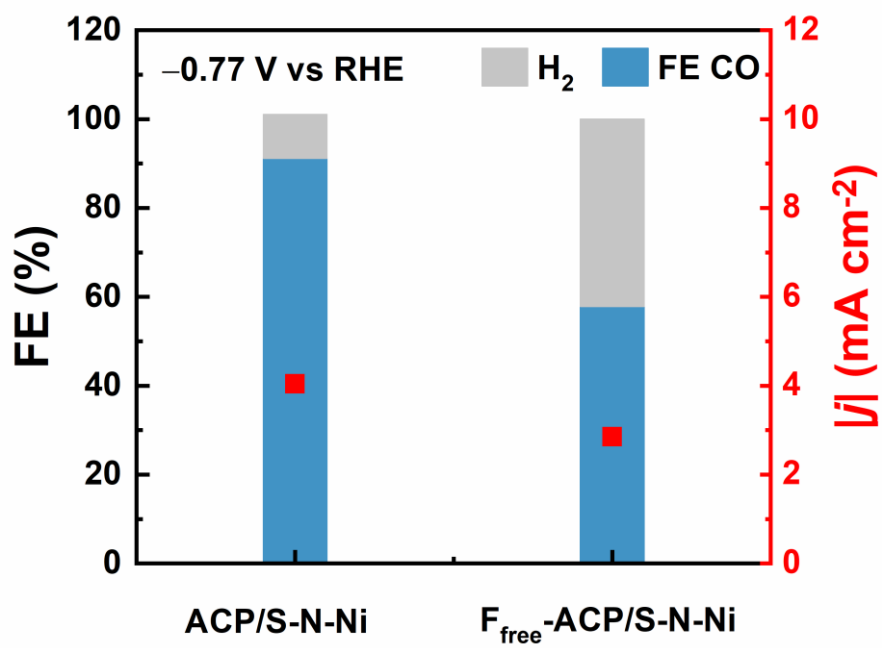
Figure S16. FE and $|j|$ measured at -0.77 V vs RHE for ACP/S-N-Ni and F_{free}-ACP/S-N-Ni after 15 min electrolysis in CO_2-saturated 0.5 M $KHCO_3$.

Table S1. **Fitting EXAFS Data Using Different Structures Based on DFT Calculations.**[a],[b]

Hypothetic structure (DFT)	E_{surface} (eV) [c]	Formation energy (eV)	Shell	Coordination Number	Interatomic distance /Å (DFT)	$\Delta\sigma^2$ (Å^2) [d]	R-factor[e]
N$_4$-Ni	−267.68	1.92	Ni-N	4	1.89078	0.0006	0.0850
N$_3$S-Ni	−260.89	5.11	Ni-N	3	1.87935	0.0100	0.0060
			Ni-S	1	1.93873		
NSNS-Ni	−253.63	8.77	Ni-N	2	1.95214	0.1020	0.0300
			Ni-S	2	1.86214		
NNSS-Ni	−252.79	9.61	Ni-N	2	1.79408	0.0100	0.0150
			Ni-S	2	1.99755		
NS$_3$-Ni	−245.33	13.47	Ni-N	1	1.81608	0.0020	0.0100
			Ni-S	3	1.92566		
S$_4$-Ni	−236.67	18.53	Ni-S	4	1.89784	0.0070	0.0400

[a] The data range adopted for data fitting in k-space and R-space are 3–10 and 1–3 Å, respectively.
[b] DFT: density functional theory.
[c] E_{surface}: energy of doped graphene surfaces
[d] $\Delta\sigma^2$: Debye-Waller factor.
[e] R-factor: a measure of the deviation between the experimental data and the fitting.

Table S2. Elemental Composition of Different Electrodes Determined by XPS.

Electrode	C (at %)	F (at %)	O (at %)	S (at %)	N (at %)	Ni (at %)
CP	46.3±0.6	53.5±0.8	0.2±0.2			
ACP	45.5±1.1	47.1±0.8	5.7±0.4	1.7±0.4		
ACP-Ni^{2+}	49.2±0.7	49.3±0.9	1.5±0.3	[a]		
CP/N-Ni	97.0±0.1		2.1±0.1		0.9±0.1	
ACP/S	98.2±0.3		1.6±0.3	0.2±0.1		
ACP/S-N	96.8±0.6		2.2±0.5	0.2±0.1	0.8±0.1	
ACP/S-Ni	97.0±0.4		2.7±0.5	0.2±0.1		0.1±0.01
ACP/S-N-Ni	95.4±0.5		2.8±0.5	0.3±0.1	1.2±0.2	0.3±0.1

[a] Amount of S in ACP-Ni^{2+} could not be determined because of overlaying F and C signals in the XPS survey spectrum. The high-resolution S 2p spectrum proves the presence of S.

ICP-OES was employed to determine the metal content in the electrodes containing Ni, as this technique is more accurate than XPS.

Table S3. Metal Content in Different Electrodes Determined by ICP-OES.

Electrode	Electrode area (cm^2) [a]	Electrode mass (mg)	Ni mass on electrode (mg)	Ni loading ($mg\ cm^{-2}$)	Ni content (wt %)
ACP/S-Ni	$1 \times 0.5 \times 2$	1.99	0.0118	0.0118	0.59
ACP/S-N-Ni	$1 \times 0.5 \times 2$	2.23	0.0234	0.0234	1.04

[a] Includes both sides of an electrode with an area of $1 \times 0.5\ cm^2$.

Table S4. Comparison of the Performance of ACP/S-N-Ni with Other Single Atom Catalysts and Supported Molecular Complexes for eCO$_2$RR.

	Electrocatalyst[a]	Cathode material	ICP wt%	Mass loading (mg cm^{-2})	Metal loading (mg cm^{-2})	FE$_{CO}$ (%)[b]	η (mV) [c]	$|j|$ (mA cm^{-2}) [d]	C_{dl} (mF cm^{-2})	ref
I	CoTPP-CNT[e]	Glassy carbon	N/A	N/A	N/A	91	550	3.2	N/A	S5
	COF-367-Co[f]	Carbon fibric	1.00	N/A	N/A	90	550	3.3	N/A	S6
	CoPPc/CNT[g]	Carbon paper	2.60	1.00	0.0260	>80	340	~4.0	N/A	S7
	Ni-TAPc/CNTs[h]	Rotating disk electrode	0.27	0.10	0.0003	99	600	32.3	N/A	S8
	Ni(alkynyl-cyclam)	Glassy carbon	N/A	N/A	N/A	8	N/A	~1.0	N/A	S9
	Ni-cyclam	Glassy carbon	N/A	N/A	N/A	91	N/A	~0.2	N/A	S10
	Fe-PB[i]	Glassy carbon	N/A	0.14	N/A	100	520	~0.4	N/A	S11
II	Fe-CNPs-w/o	Carbon cloth	N/A	1.00	N/A	98	470	~2.5	3.1	S12
	Fe-N-C	Glassy carbon	N/A	0.46	N/A	93	390	~6.0	N/A	S13
	STPYP-Co	Carbon paper	N/A	0.12	N/A	96	500	6.5	N/A	S14
	Co-N5/HNPCSs	Carbon paper	3.54	N/A	N/A	99	680	10.2	N/A	S15
	Zn-N-G-800	Carbon cloth	N/A	2.00	N/A	90	390	~4.5	21.9	S16
	SACs Ni-N-C	Carbon paper	1.53	0.10	0.0015	72	890	10.5	N/A	S17
	NiSA-N-CNTs	Carbon paper	20.00	1.00	0.2000	91	N/A	23.5	N/A	S18
	A-Ni-NSG	Glassy carbon rotating disk electrode	2.80	0.1	0.0028	97	610	22.0	8.3	S19
	Ni-N-C	Carbon paper	N/A	0.60	N/A	97	640	~7.5	30.9	S20
III	NiSA/PCFM[j]	Electrospin-ning membrane	N/A	N/A	N/A	96	590	~13	20.2	S21
	ACP/S-N-Ni	**Carbon paper**	**1.04**	**/**	**0.02**	**91**	**660**	**4.1**	**1.54**	**This work**

[a] Electrocatalyst are categorized into three types, i.e. I: supported molecular catalysts or metal-organic complexes, II: powder single atom catalysts, III: self-supported single atom catalysts.

[b] Maximum FE$_{CO}$ in the reports.

[c] Overpotential at which the maximum FE$_{CO}$ is achieved.

[d] Current density achieved at the listed overpotential.

[e] Cobalt meso-tetraphenylporphyrin on carbon nanotubes.

[f] COF: covalent organic framework.

[g] Cobalt polyphthalocyanine-sheathed carbon nanotubes.

[h] Nickel(II) 2,9,16,23-tetra(amino)phthalocyanine on carbon nanotubes.

[i] PB: porphyrin box, which was synthesized by condensing six tetraformylphenylporphyrins and eight triamine linkers.

[j] PCFM: porous carbon fiber membrane.

References

S1.   Z. Wang, Y. Dong, H. Li, Z. Zhao, H. B. Wu, C. Hao, S. Liu, J. Qiu and X. W. D. Lou, *Nat. Commonl.*, 2014, **5**, 1–8.

S2.   L. Zhang, L. Ji, P.-A. Glans, Y. Zhang, J. Zhu and J. Guo, *Phys. Chem. Chem. Phys.*, 2012, **14**, 13670–13675.

S3.   P. Huang, M. Cheng, H. Zhang, M. Zuo, C. Xiao and Y. Xie, *Nano Energy.*, 2019, **61**, 428–434.

S4.   M. Kim, S. Lee and B. Kang, *Adv. Sci.*, 2016, **3**, 1500366.

S5.   X. M. Hu, M. H. Ronne, S. U. Pedersen, T. Skrydstrup and K. Daasbjerg, *Angew Chem Int Ed.*, 2017, **56**, 6468–6472.

S6.   S. Lin, C. S. Diercks, Y.-B. Zhang, N. Kornienko, E. M. Nichols, Y. Zhao, A. R. Paris, D. Kim, P. Yang and O. Yaghi, *Science.*, 2015, **349**, 1208–1213.

S7.   N. Han, Y. Wang, L. Ma, J. Wen, J. Li, H. Zheng, K. Nie, X. Wang, F. Zhao, Y. Li, J. Fan, J. Zhong, T. Wu, D. J. Miller, J. Lu, S.-T. Lee and Y. Li, *Chem.*, 2017, **3**, 652–664.

S8.   S. Liu, H. B. Yang, S. F. Hung, J. Ding, W. Cai, L. Liu, J. Gao, X. Li, X. Ren, Z. Kuang, Y. Huang, T. Zhang and B. Liu, *Angew Chem Int Ed.*, 2020, **59**, 798–803.

S9.   A. Zhanaidarova, C. E. Moore, M. Gembicky and C. P. J. C. C. Kubiak, *Chem. Commun.*, 2018, **54**, 4116–4119.

S10. E. M. Nichols and C. Chang, *Organometallics.*, 2018, **38**, 1213–1218.

S11. P. T. Smith, B. P. Benke, Z. Cao, Y. Kim, E. M. Nichols, K. Kim and C. J. Chang, *Angew Chem Int Ed.*, 2018, **57**, 9684–9688.

S12. C. Hu, S. Bai, L. Gao, S. Liang, J. Yang, S. D. Cheng, S. B. Mi and J. Qiu, *ACS Catal.*, 2019, **9**, 11579–11588.

S13. X. Qin, S. Zhu, F. Xiao, L. Zhang and M. Shao, *ACS Energy Lett.*, 2019, **4**, 1778–1783.

S14. J. Han, P. An, S. Liu, X. Zhang, D. Wang, Y. Yuan, J. Guo, X. Qiu, K. Hou, L. Shi, Y. Zhang, S. Zhao, C. Long and Z. Tang, *Angew Chem Int Ed.*, 2019, **58**, 12711–12716.

S15. Y. Pan, R. Lin, Y. Chen, S. Liu, W. Zhu, X. Cao, W. Chen, K. Wu, W.-C. Cheong and Y. Wang, *J. Am. Chem. Soc.*, 2018, **140**, 4218–4221.

S16. Z. Chen, K. Mou, S. Yao and L. Liu, *ChemSusChem*, 2018, **11**, 2944–2952.

S17. C. Zhao, X. Dai, T. Yao, W. Chen, X. Wang, J. Wang, J. Yang, S. Wei, Y. Wu and Y. Li, *J. Am. Chem. Soc.*, 2017, **139**, 8078–8081.

S18. Y. Cheng, S. Zhao, B. Johannessen, J. P. Veder, M. Saunders, M. R. Rowles, M. Cheng, C. Liu, M. F. Chisholm and R. De Marco, *Adv. Mater.*, 2018, **30**, 1706287.

S19. H. B. Yang, S.-F. Hung, S. Liu, K. Yuan, S. Miao, L. Zhang, X. Huang, H.-Y. Wang, W. Cai, R. Chen, J. Gao, X. Yang, W. Chen, Y. Huang, H. M. Chen, C. M. Li, T. Zhang and B. Liu, *Nature Energy*, 2018, **3**, 140–147.

S20. F. Pan, H. Zhang, Z. Liu, D. Cullen, K. Liu, K. More, G. Wu, G. Wang and Y. Li, *J. Mater. Chem. A.*, 2019, **7**, 26231–26237.

S21. H. Yang, Q. Lin, C. Zhang, X. Yu, Z. Cheng, G. Li, Q. Hu, X. Ren, Q. Zhang, J. Liu and C. He, *Nat. Commun.*, 2020, **11**, 593.